

Optimization-Based Velocity-Integral Sliding-Window Coarse Alignment: Attitude Error Analysis and Validation

Xuyang Jiang

Abstract—The optimization-based alignment (OBA) approach transforms the strapdown inertial navigation system (SINS) coarse alignment into a constant initial attitude estimation problem, serving as a prevalent technique for global navigation satellite system (GNSS)-aided in-motion alignment. While existing studies focus on improving accuracy by refining attitude determination algorithms or constructing robust observation vectors, a rigorous analytical mapping to evaluate the resulting attitude errors from raw sensor and aiding-velocity uncertainties has yet to be established for fixed-length sliding-window velocity-integral OBA. To address this issue, this paper proposes a first-order attitude error propagation model for GNSS-aided sliding-window velocity-integral OBA. Specifically, a sliding-window observation model and its discrete implementation are formulated, through which gyroscope errors, accelerometer errors, GNSS velocity noise, and lever-arm effects are analytically propagated to non-normalized observation vectors. Subsequently, Davenport's q method is used to establish the mapping from these vector perturbations to attitude misalignment. By decoupling systematic errors and stochastic noise, the deterministic attitude offsets and the attitude error covariances are respectively derived. Monte Carlo simulations demonstrate that the analytical model accurately captures the deterministic attitude offsets and precisely characterizes the statistical spread, yielding standard-deviation ratios between 0.929 and 1.060 with empirical coverage above 99.4%. Vehicle field tests further confirm its practical applicability, showing that the predicted covariance envelopes reliably bound the actual initial-attitude errors, with steady-state RMSEs strictly below 0.00495 deg. These results validate the proposed model for coarse-alignment attitude error assessment.

Index Terms—strapdown inertial navigation system, coarse alignment, optimization-based alignment, sliding window, error propagation, attitude error covariance

I. INTRODUCTION

STRAPDOWN inertial navigation system (SINS) propagates attitude, velocity, and position without continuous external measurements and is fundamental to terrestrial, surface vessel, airborne, and underwater navigation systems [1], [2]. As a dead-reckoning system, a SINS must be initialized with reliable navigation states. Velocity and position are typically provided by external sensors such as the global navigation satellite system (GNSS), Doppler velocity log (DVL), or odometer, whereas the initial attitude must be determined by alignment. Fine alignment usually relies on an extended

Kalman filter (EKF), whose linearized error model is valid only when the attitude misalignment is sufficiently small. Although nonlinear filters such as cubature, unscented, and particle filters can handle large initial misalignments, they usually require more computation and more delicate parameter tuning [3]. Therefore, an accurate and robust coarse alignment remains an indispensable prerequisite. Beyond merely estimating the initial attitude, practical implementation requires a reliable error covariance to initialize the subsequent fine-alignment filters. Thus, an error evaluation model that explicitly decouples individual error sources is as critical as the alignment algorithm itself.

SINS coarse alignment can be fundamentally interpreted as a multi-vector attitude determination problem. Classical analytical coarse alignment is closely related to spacecraft attitude determination, where vector observations are used to determine a direction cosine matrix (DCM). The TRIaxial Attitude Determination (TRIAD) algorithm pioneered the deterministic solution for basic two-vector observations. For redundant multi-vector cases, Wahba's problem formulates this task as a least-squares optimization over attitude matrices. Representative solvers include singular value decomposition (SVD), the fast optimal attitude matrix (FOAM), Davenport's q method, quaternion estimator (QUEST), and estimator of the optimal quaternion (ESOQ) methods [4], [5]. More recently, the fast linear attitude estimator (FLAE) transformed the quaternion attitude determination problem into a linear form and further improved computational efficiency [6]. These methods provide the mathematical foundation for multi-vector attitude determination.

Since this multi-vector framework was originally pioneered for spacecraft attitude determination using star trackers, adapting it to coarse alignment requires constructing alternative observation vectors from navigation kinematics. To bridge this gap, early studies used the apparent drift of gravity in the inertial frame or aided velocity measurements to construct vector pairs for attitude or mounting-angle estimation [7]–[9]. Wu and Silson then independently introduced optimization-based alignment (OBA) and velocity-loci alignment, respectively, showing that apparent velocity vectors accumulated over multiple epochs can transform coarse alignment into a constant initial attitude estimation problem [10], [11]. Compared with analytical coarse alignment, this accumulation improves redundancy and strengthens maneuver-dependent observability. Wu further analyzed the global observability of SINS alignment under suitable maneuvers from a non-

Xuyang Jiang is with the School of Instrument Science and Engineering, Southeast University, Nanjing, China (e-mail: jxy@seu.edu.cn).

linear constraint perspective [12]. For GNSS-aided in-motion scenarios, Wu integrated standard SINS coning and sculling algorithms into the velocity integration formulation, thereby enabling a rigorous discrete velocity-integral OBA for in-flight coarse alignment [13].

Subsequent studies have improved OBA along several complementary directions. Li and Yue introduced filtering or dynamic sliding-window strategies to mitigate the effects of swaying-base motion and reduce observation-vector errors [14], [31]. Wu, Chang, and Huang incorporated gyroscope bias, accelerometer bias, lever-arm parameters, and body-attitude propagation errors into online optimization, nonlinear filtering, or EKF closed-loop feedback frameworks for GNSS- and odometer-aided SINS coarse alignment [15]–[19]. For low-cost inertial sensors and degraded aiding velocity, Yao, Xu, and Zhou further exploited kinematic constraints, vector subtraction, magnitude matching, robust weighting, and sliding-window optimization to improve robustness against velocity anomalies and degraded motion excitation [20]–[25]. More recent work has extended the formulation itself through filtering based on the vectorized Davenport matrix, factor graph optimization (FGO), and equivalent backtracking, as well as by employing Lie-group invariant-error descriptions for complex dynamics and large-misalignment conditions [26]–[30]. Taken together, these studies indicate that the attitude error of sliding-window velocity-integral OBA is jointly determined by deterministic sensor errors, stochastic sensor noise, aiding-velocity errors, lever-arm effects, and motion excitation. Consequently, providing solely an attitude estimate without quantifying its underlying uncertainty is inadequate for comprehensively assessing alignment reliability.

Despite these algorithmic advancements, error propagation analysis for OBA remains insufficiently addressed, particularly regarding the limitations of underlying mathematical assumptions. For general attitude determination, Shuster proposed the TASTE test for unit-vector observation consistency [32]. Meanwhile, Markley and Crassidis analyzed the covariance of Wahba, QUEST, and Davenport-type methods under normalized-vector and zero-mean Gaussian assumptions [4]. For SINS alignment, Silson derived covariance expressions for stationary velocity-loci alignment, while Wu developed a linear error model for gyroscope bias, accelerometer bias, and lever-arm effects [11], [15]. Within the classical analytical alignment framework, Silva derived generalized error equations for stationary SINS, separating normalization and non-orthogonality effects to analytically estimate horizontal gyroscope and vertical accelerometer biases [33]–[35]. To address non-normalized observations, Chang analyzed Davenport’s q-method error propagation using pseudo-inverse-based eigenvector perturbation, Cheng extended attitude estimation to pose estimation with covariance analysis, and Ouyang and Wu developed covariance analyses for stationary, odometer-aided, and GNSS-aided OBA scenarios [36]–[38]. Nonetheless, these derivations either rely on normalized unit-vector assumptions, focus on stationary or weakly dynamic cases, or require raw measurement errors to be mutually independent and strictly zero-mean Gaussian. Consequently, sliding-window velocity-integral OBA still lacks an explicit

description of how deterministic attitude offsets, stochastic error covariance, accumulated attitude propagation errors, and window endpoint differencing are coupled under complex in-motion conditions.

To address this issue, this paper develops a first-order analytical propagation model for mapping raw measurement errors to attitude-error statistics for GNSS-aided sliding-window velocity-integral OBA. The main contributions are summarized as follows:

- A nominal sliding-window velocity-integral OBA observation model and its discrete implementation are derived to identify the roles of specific-force integration, velocity endpoint differencing, and attitude-chain projection.
- Raw inertial measurement unit (IMU) errors, GNSS velocity errors, and lever-arm effects are propagated to non-normalized observation-vector errors, while deterministic attitude offsets and stochastic error covariance are treated separately.
- Based on Davenport’s q method, a first-order analytical mapping from observation-vector perturbations to attitude misalignment and covariance is established and validated by Monte Carlo simulation and a vehicle field test.

The remainder of this paper is organized as follows. Section II presents the sliding-window velocity-integral OBA model, discretization, and Wahba-Davenport solution. Section III derives the error propagation model. Section IV verifies the model by simulation. Section V presents a vehicle field-test validation, and Section VI concludes the paper.

II. SLIDING-WINDOW VELOCITY-INTEGRAL OBA

A. Continuous Observation Model

By convention, the east-north-up (ENU) navigation frame is denoted by n , and the right-forward-up (RFU) body frame by b . Accordingly, the navigation-frame velocity is

$$\mathbf{v}^n = [v_E, v_N, v_U]^T. \quad (1)$$

With the initial alignment epoch $t = 0$ as the reference, the attitude matrix at any time t can be decomposed as

$$C_b^n(t) = C_{n(0)}^{n(t)} C_b^n(0) C_{b(t)}^{b(0)}, \quad (2)$$

where $C_b^n(0)$ is the constant unknown initial attitude matrix. The matrices $C_{b(t)}^{b(0)}$ and $C_{n(0)}^{n(t)}$ denote the attitude changes of the body and navigation frames over $[0, t]$, respectively. Their time evolutions are governed by

$$\dot{C}_{b(t)}^{b(0)} = C_{b(t)}^{b(0)} [\boldsymbol{\omega}_{ib}^b \times], \quad \dot{C}_{n(0)}^{n(t)} = C_{n(0)}^{n(t)} [\boldsymbol{\omega}_{in}^n \times]. \quad (3)$$

The differential equations in (3) can be numerically solved by integrating the gyroscope-measured body angular rate and the velocity-derived navigation angular rate. The SINS velocity equation is

$$\dot{\mathbf{v}}^n = C_b^n \mathbf{f}^b - (2\boldsymbol{\omega}_{ie}^n + \boldsymbol{\omega}_{en}^n) \times \mathbf{v}^n + \mathbf{g}^n, \quad (4)$$

where \mathbf{f}^b is specific force, \mathbf{g}^n is gravity, and $\boldsymbol{\omega}_{ie}^n$ and $\boldsymbol{\omega}_{en}^n$ are the Earth rotation rate and transport rate expressed in the navigation frame. Substituting (2) into (4) and integrating

over the sliding window $[t_m, t]$ yield the sliding-window OBA observation relation

$$C_b^n(0)\boldsymbol{\alpha}(t) = \boldsymbol{\beta}(t), \quad (5)$$

where the body-side observation vector is

$$\boldsymbol{\alpha}(t) = \int_{t_m}^t C_{b(\tau)}^{b(0)} \mathbf{f}^b(\tau) d\tau, \quad (6)$$

and the navigation-side reference vector is

$$\begin{aligned} \boldsymbol{\beta}(t) &= C_{n(t)}^{n(0)} \mathbf{v}^n(t) - C_{n(t_m)}^{n(0)} \mathbf{v}^n(t_m) \\ &+ \int_{t_m}^t C_{n(\tau)}^{n(0)} [\boldsymbol{\omega}_{ie}^n(\tau) \times \mathbf{v}^n(\tau) - \mathbf{g}^n(\tau)] d\tau. \end{aligned} \quad (7)$$

Equations (5)–(7) are consistent with the constant-attitude constraint in classical OBA. The velocity-integral observation construction follows the OBA and velocity integration formulation in [10], [13]. The key distinction is that each observation vector is constructed in a fixed-length sliding window rather than by an integral starting from the initial alignment time. This limits the integration length of a single observation vector and suppresses the long-term accumulation of accelerometer errors. Nevertheless, the integrated attitude matrix $C_{b(\tau)}^{b(0)}$ within each window inherently retains the gyroscope errors accumulated prior to the window start.

B. Discrete Implementation

Let $t_k = kT$ be the discrete sampling epoch, where T denotes the update period, and let the fixed-length sliding window $[t_m, t_M]$ correspond to the discrete indices m to M . The discrete implementation in (8)–(13) adopts the dual-sample coning/sculling form used in velocity-integral OBA [13]. The dual-sample gyroscope angle increments and accelerometer velocity increments within one update period are denoted by $\Delta\boldsymbol{\theta}_{1,k}$, $\Delta\boldsymbol{\theta}_{2,k}$, $\Delta\mathbf{v}_{1,k}$, and $\Delta\mathbf{v}_{2,k}$. The body-frame equivalent rotation vector with coning compensation is

$$\boldsymbol{\varphi}_{b,k} = \Delta\boldsymbol{\theta}_{1,k} + \Delta\boldsymbol{\theta}_{2,k} + \frac{2}{3}\Delta\boldsymbol{\theta}_{1,k} \times \Delta\boldsymbol{\theta}_{2,k}. \quad (8)$$

Let $\varphi_{b,k} = \|\boldsymbol{\varphi}_{b,k}\|$. The single-step attitude increment is obtained from Rodrigues' formula,

$$\begin{aligned} C_{b(t_{k+1})}^{b(t_k)} &= I + \frac{\sin \varphi_{b,k}}{\varphi_{b,k}} [\boldsymbol{\varphi}_{b,k} \times] \\ &+ \frac{1 - \cos \varphi_{b,k}}{\varphi_{b,k}^2} [\boldsymbol{\varphi}_{b,k} \times]^2. \end{aligned} \quad (9)$$

The accumulated body attitude is propagated by

$$C_{b(t_{k+1})}^{b(0)} = C_{b(t_k)}^{b(0)} C_{b(t_{k+1})}^{b(t_k)}. \quad (10)$$

The navigation-frame attitude matrix $C_{n(t_k)}^{n(0)}$ is propagated analogously using $\boldsymbol{\omega}_{in}^n = \boldsymbol{\omega}_{ie}^n + \boldsymbol{\omega}_{en}^n$. The specific-force integral uses dual-sample rotation and sculling compensation:

$$\begin{aligned} \Delta\mathbf{v}_{c,k} &= \Delta\mathbf{v}_{1,k} + \Delta\mathbf{v}_{2,k} \\ &+ \frac{1}{2}(\Delta\boldsymbol{\theta}_{1,k} + \Delta\boldsymbol{\theta}_{2,k}) \times (\Delta\mathbf{v}_{1,k} + \Delta\mathbf{v}_{2,k}) \\ &+ \frac{2}{3}(\Delta\boldsymbol{\theta}_{1,k} \times \Delta\mathbf{v}_{2,k} + \Delta\mathbf{v}_{1,k} \times \Delta\boldsymbol{\theta}_{2,k}). \end{aligned} \quad (11)$$

The discrete observation vectors of the i th sliding window are then

$$\boldsymbol{\alpha}_i = \sum_{k=m_i}^{M_i-1} C_{b(t_k)}^{b(0)} \Delta\mathbf{v}_{c,k}, \quad (12)$$

and

$$\begin{aligned} \boldsymbol{\beta}_i &= C_{n(t_{M_i})}^{n(0)} \mathbf{v}^n(t_{M_i}) - C_{n(t_{m_i})}^{n(0)} \mathbf{v}^n(t_{m_i}) \\ &+ \sum_{k=m_i}^{M_i-1} C_{n(t_k)}^{n(0)} [\boldsymbol{\omega}_{ie}^n(t_k) \times \mathbf{v}^n(t_k) - \mathbf{g}^n(t_k)] T. \end{aligned} \quad (13)$$

C. Wahba-Davenport Attitude Solution

Given multiple sliding-window observation pairs $(\boldsymbol{\alpha}_i, \boldsymbol{\beta}_i)$, the weighted Wahba problem over the special orthogonal group $SO(3)$ is

$$\hat{C} = \arg \min_{C \in SO(3)} \sum_{i=1}^N w_i \|\boldsymbol{\beta}_i - C\boldsymbol{\alpha}_i\|^2. \quad (14)$$

Here $SO(3)$ denotes the set of proper three-dimensional rotation matrices. This paper directly uses non-normalized velocity-integral observation vectors in (14); $\boldsymbol{\alpha}_i$ and $\boldsymbol{\beta}_i$ are not normalized to unit vectors. Consequently, their magnitudes directly reflect the local motion excitation and signal-to-noise ratio within each sliding window, thereby implicitly assigning higher weights to the more informative observation vectors. Accordingly, the nominal implementation simply adopts a uniform weight $w_i = 1$ for all windows. Mathematically, applying an arbitrary common scalar weight across all windows merely scales the objective function (14) proportionally, yielding the identical optimal attitude solution.

Define the attitude profile matrix, antisymmetric vector, and Davenport gain matrix as

$$B = \sum_{i=1}^N w_i \boldsymbol{\beta}_i \boldsymbol{\alpha}_i^T, \quad \mathbf{Z} = \sum_{i=1}^N w_i \boldsymbol{\beta}_i \times \boldsymbol{\alpha}_i, \quad (15)$$

$$K = \begin{bmatrix} \text{tr}(B) & \mathbf{Z}^T \\ \mathbf{Z} & B + B^T - \text{tr}(B)I_3 \end{bmatrix}. \quad (16)$$

Using a scalar-first unit quaternion $q = [s, \boldsymbol{\eta}^T]^T$, (14) is equivalent to

$$\hat{q} = \arg \max_{q^T q = 1} q^T K q. \quad (17)$$

Therefore, \hat{q} is the unit eigenvector associated with the largest eigenvalue of K . To establish a direct equivalence between this Davenport formulation and the residual-minimization OBA formulation in [38], the homogeneous residual normal matrix can be written as $K_{\text{OBA}} = cI_4 - 2K$, where $c = \sum_i w_i (\|\boldsymbol{\alpha}_i\|^2 + \|\boldsymbol{\beta}_i\|^2)$. Since c is a scalar constant, solving for the largest-eigenvalue eigenvector of K yields the same optimal attitude as solving for the smallest-eigenvalue eigenvector of K_{OBA} .

III. ERROR PROPAGATION MODEL

A. From Raw Errors to Observation-Vector Errors

Following the convention that the measurement error is defined as the measured value minus the true value, the gyroscope, accelerometer, and GNSS velocity measurement models are

$$\begin{aligned}\tilde{\omega}_{ib}^b &= \omega_{ib}^b + \delta\omega_{ib}^b, & \delta\omega_{ib}^b &= \epsilon^b + \mathbf{w}_g, \\ \tilde{\mathbf{f}}^b &= \mathbf{f}^b + \delta\mathbf{f}^b, & \delta\mathbf{f}^b &= \nabla^b + \mathbf{w}_a, \\ \tilde{\mathbf{v}}_{GNSS}^n &= \mathbf{v}_{GNSS}^n + \delta\mathbf{v}_{GNSS}^n, & \delta\mathbf{v}_{GNSS}^n &= \mathbf{w}_v.\end{aligned}\quad (18)$$

Here ϵ^b and ∇^b are constant gyroscope and accelerometer biases, while \mathbf{w}_g , \mathbf{w}_a , and \mathbf{w}_v are stochastic noise terms. If \mathbf{l}^b denotes the lever arm from the IMU measurement center to the GNSS antenna phase center, the GNSS antenna velocity and the IMU-center velocity satisfy

$$\begin{aligned}\tilde{\mathbf{v}}_{GNSS}^n &= \mathbf{v}^n + \delta\mathbf{v}_{GNSS}^n + C_b^n(\omega_{eb}^b \times \mathbf{l}^b), \\ \omega_{eb}^b &= \omega_{ib}^b - C_n^b\omega_{ie}^n.\end{aligned}\quad (19)$$

To describe accumulated attitude projection errors uniformly, the computed projection matrix of any rotating frame x is assumed to have a right-multiplicative small misalignment ϕ^x :

$$\tilde{C}_{x(\tau)}^{x(0)} \approx C_{x(\tau)}^{x(0)} (I + [\phi^x(\tau) \times]). \quad (20)$$

With angular-rate error $\delta\omega^x$ and neglecting second-order small terms,

$$\dot{\phi}^x = \delta\omega^x - \omega^x \times \phi^x, \quad \phi^x(\tau) = \int_0^\tau C_{x(s)}^{x(\tau)} \delta\omega^x(s) ds. \quad (21)$$

For the body side, set $x = b$ and $\delta\omega^x = \delta\omega_{ib}^b$. Taking the first-order variation of the nominal specific-force integral in (6) and using (20) to separate projection-matrix errors, the body-side observation-vector error decomposes into the direct integral of accelerometer errors and the accumulated attitude projection perturbation induced by gyroscope errors:

$$\delta\alpha_{a,i} = \int_{t_{m_i}}^{t_{M_i}} C_{b(\tau)}^{b(0)} \delta\mathbf{f}^b(\tau) d\tau, \quad (22)$$

$$\delta\alpha_{g,i} = - \int_{t_{m_i}}^{t_{M_i}} C_{b(\tau)}^{b(0)} [\mathbf{f}^b(\tau) \times \phi^b(\tau)] d\tau. \quad (23)$$

Equation (23) reveals a fundamental advantage of the sliding-window scheme. In traditional OBA, integrating from the initial alignment time causes late-stage observation vectors to grow continuously in magnitude. Since the unweighted Wahba problem implicitly favors vectors with larger magnitudes, observations near the end of the alignment interval may dominate the attitude solution while also carrying the most severe accumulated gyroscope errors. By restricting the integration to a fixed length, the sliding-window approach bounds the vector magnitudes to reflect local motion intensity rather than the accumulated alignment time. This prevents heavily corrupted late-stage observations from disproportionately dominating the unweighted objective function.

On the navigation side, velocity errors affect $C_{n(\tau)}^{n(0)}$ through the transport rate. Under the ENU convention,

$$\delta\omega_{en}^n = M_v \delta\mathbf{v}_{GNSS}^n, \quad M_v = \begin{bmatrix} 0 & -\frac{1}{R_M + h} & 0 \\ \frac{1}{R_N + h} & 0 & 0 \\ \frac{\tan L}{R_N + h} & 0 & 0 \end{bmatrix}. \quad (24)$$

During coarse alignment, ω_{ie}^n is determined by the known latitude. The effect of position error on the projection of Earth rotation is much smaller than the effect of velocity error on ω_{en}^n , so $\delta\omega_{in}^n \approx \delta\omega_{en}^n = M_v \delta\mathbf{v}_{GNSS}^n$. The resulting ϕ^n can be obtained from (21). A first-order expansion of (7) reveals that the dominant GNSS velocity error contribution emerges as an endpoint difference

$$\delta\beta_{v,i} \approx C_{n(t_{M_i})}^{n(0)} \delta\mathbf{v}_{GNSS}^n(t_{M_i}) - C_{n(t_{m_i})}^{n(0)} \delta\mathbf{v}_{GNSS}^n(t_{m_i}). \quad (25)$$

Compared with endpoint velocity differencing, the integral terms associated with $\omega_{ie}^n \times \delta\mathbf{v}_{GNSS}^n$ and ϕ^n are bounded by the Earth's rotation rate and its radii of curvature, and are thus treated as higher-order small terms in the discrete implementation. This approximation is suitable for short-window coarse alignment and degree- to subdegree-level attitude error assessment. For long-duration integration or arcminute/sub-arcminute accuracy requirements, these coupling terms should be strictly retained in the analytical model or estimated via numerical integration.

The lever-arm effect initially enters through the GNSS velocity observation in the β -side sliding-window integral. Integrating this effect over the sliding window and invoking the attitude-chain relation in (2) equivalently transfers its contribution to the α side. The resulting dominant term manifests as an endpoint difference:

$$\begin{aligned}\delta\alpha_{l,i} &\approx C_{b(t_{M_i})}^{b(0)} [\omega_{eb}^b(t_{M_i}) \times \mathbf{l}^b] \\ &\quad - C_{b(t_{m_i})}^{b(0)} [\omega_{eb}^b(t_{m_i}) \times \mathbf{l}^b].\end{aligned}\quad (26)$$

The equivalent observation-vector errors entering the Wahba-Davenport solution are

$$\delta\alpha_i = \delta\alpha_{a,i} + \delta\alpha_{g,i} - \delta\alpha_{l,i}, \quad \delta\beta_i = \delta\beta_{v,i}. \quad (27)$$

B. From Observation-Vector Errors to Attitude Error

In the error-free case, the largest eigenvalue and its unit quaternion of the Davenport matrix satisfy

$$Kq_1 = \lambda_1 q_1, \quad q_1^T q_1 = 1, \quad \lambda_1 = \lambda_{\max}(K). \quad (28)$$

Let δK be the first-order Davenport matrix perturbation caused by observation-vector errors. The additive quaternion error in (29) follows the first-order Davenport q-method error analyses in [36], [38]. It is obtained by linearizing the perturbed eigenvalue equation $(K + \delta K)(q_1 + \delta q_1) = (\lambda_1 + \delta\lambda_1)(q_1 + \delta q_1)$ and applying the unit-norm constraint $q_1^T \delta q_1 = 0$:

$$\delta q_1 = (\lambda_1 I_4 - K + q_1 q_1^T)^{-1} (I_4 - q_1 q_1^T) \delta K q_1. \quad (29)$$

When the largest eigenvalue is non-repeated, i.e., has an algebraic multiplicity of one, $\lambda_1 I_4 - K + q_1 q_1^T$ is nonsingular,

avoiding the need for an explicit pseudoinverse. Let $q_1 = [s_1, \boldsymbol{\eta}_1^T]^T$. Assuming deterministic errors and stochastic noise are small, the true attitude remains in a local neighborhood of the nominal Davenport solution, and large-misalignment nonlinear perturbations can be neglected. In this case, to link the four-dimensional algebraic quaternion perturbation to the three-dimensional physical attitude error, a multiplicative error quaternion Δq is introduced. The perturbed quaternion can be equivalently expressed in additive and multiplicative forms as $q_1 + \delta q_1 = q_1 \odot \Delta q$, where \odot denotes quaternion multiplication. Applying the small-angle approximation $\Delta q \approx [1, \frac{1}{2}\delta\boldsymbol{\theta}^T]^T$ and expanding the quaternion product yields $q_1 \odot \Delta q \approx q_1 + \frac{1}{2}\Xi(q_1)\delta\boldsymbol{\theta}$. Comparing the two forms, the additive quaternion perturbation is linearly related to the attitude error vector by $\delta q_1 \approx \frac{1}{2}\Xi(q_1)\delta\boldsymbol{\theta}$. Since $\Xi(q_1)^T\Xi(q_1) = I_3$, left-multiplying both sides by $2\Xi(q_1)^T$ yields

$$\delta\boldsymbol{\theta} = 2\Xi(q_1)^T\delta q_1, \quad \Xi(q_1)^T = [-\boldsymbol{\eta}_1 \quad s_1 I_3 + [\boldsymbol{\eta}_1 \times]]. \quad (30)$$

Vectorizing the perturbation matrix δK in (29) and substituting it into (30) produce the first-order mapping from Davenport matrix perturbation to three-dimensional attitude error:

$$\delta\boldsymbol{\theta} = \Phi \text{vec}(\delta K), \quad (31)$$

where $\text{vec}(\cdot)$ denotes the column-stacking matrix vectorization operator, \otimes represents the Kronecker product, and the mapping matrix Φ is given by

$$\Phi = 2\Xi(q_1)^T (\lambda_1 I_4 - K + q_1 q_1^T)^{-1} \times [q_1^T \otimes I_4 - q_1^T \otimes (q_1 q_1^T)]. \quad (32)$$

From (15) and (16), the observation-vector perturbations are related to the Davenport matrix perturbation by

$$\delta B = \sum_{i=1}^N w_i (\delta\beta_i \boldsymbol{\alpha}_i^T + \beta_i \delta\boldsymbol{\alpha}_i^T), \quad (33)$$

$$\delta \mathbf{Z} = \sum_{i=1}^N w_i (\delta\beta_i \times \boldsymbol{\alpha}_i + \beta_i \times \delta\boldsymbol{\alpha}_i), \quad (34)$$

$$\delta K = \begin{bmatrix} \text{tr}(\delta B) & \delta \mathbf{Z}^T \\ \delta \mathbf{Z} & \delta B + \delta B^T - \text{tr}(\delta B)I_3 \end{bmatrix}. \quad (35)$$

Equations (33)–(35) show that δK is linear in the observation-vector perturbations. Therefore, by vectorizing the matrix equation in (35), the linear coefficients associated with $\delta\beta_i$ and $\delta\boldsymbol{\alpha}_i$ can be explicitly extracted, and the corresponding Jacobian matrices are defined as

$$\text{vec}(\delta K) = \sum_{i=1}^N (J_{\beta,i} \delta\beta_i + J_{\alpha,i} \delta\boldsymbol{\alpha}_i) = \mathcal{J}_K \delta \mathbf{y}, \quad (36)$$

where $\delta \mathbf{y} = [\delta\beta_1^T, \delta\boldsymbol{\alpha}_1^T, \dots, \delta\beta_N^T, \delta\boldsymbol{\alpha}_N^T]^T$, $J_{\beta,i}$ and $J_{\alpha,i}$ are the Jacobian matrices of $\text{vec}(K)$ with respect to the i th observation pair, and

$$\mathcal{J}_K = [J_{\beta,1} \quad J_{\alpha,1} \quad \cdots \quad J_{\beta,N} \quad J_{\alpha,N}] \in \mathbb{R}^{16 \times 6N}. \quad (37)$$

The explicit forms of $J_{\beta,i}$ and $J_{\alpha,i}$ are derived in Appendix A. Combining (31) and (36) yields

$$\delta\boldsymbol{\theta} = \Phi \mathcal{J}_K \delta \mathbf{y}. \quad (38)$$

C. Deterministic and Stochastic Error Components

The input errors are decomposed into a deterministic component \mathcal{S} and a stochastic component \mathcal{R} :

$$\begin{aligned} \mathcal{S}: \delta\boldsymbol{\omega}_{ib}^b &= \boldsymbol{\epsilon}^b, \quad \delta\mathbf{f}^b = \nabla^b, \quad \mathbf{l}^b \neq \mathbf{0}, \\ \delta\mathbf{v}_{GNSS}^n &= \mathbf{0}, \\ \mathcal{R}: \delta\boldsymbol{\omega}_{ib}^b &= \mathbf{w}_g, \quad \delta\mathbf{f}^b = \mathbf{w}_a, \quad \mathbf{l}^b = \mathbf{0}, \\ \delta\mathbf{v}_{GNSS}^n &= \mathbf{w}_v. \end{aligned} \quad (39)$$

Equation (18) models the GNSS velocity error as zero-mean Gaussian white noise. This assumption is appropriate for high-accuracy GNSS velocity observations without significant low-frequency bias, such as real-time kinematic (RTK) or differential GNSS (DGNSS) velocity aiding. If colored noise, multipath-induced slow variation, or other low-frequency systematic components exist, they should be included in \mathcal{S} or modeled by an extended stochastic process.

The deterministic errors are treated as known constants. Their accumulated effect through all windows produces the deterministic attitude offset

$$\delta\boldsymbol{\theta}_s = \Phi \sum_{i=1}^N J_{\alpha,i} \left[\delta\boldsymbol{\alpha}_{g,i}(\boldsymbol{\epsilon}^b) + \delta\boldsymbol{\alpha}_{a,i}(\nabla^b) - \delta\boldsymbol{\alpha}_{l,i}(\mathbf{l}^b) \right]. \quad (40)$$

For the stochastic component, gyroscope-noise-induced accumulated attitude projection errors grow over time. Adjacent windows can also share endpoint GNSS velocity samples and overlapping IMU integration intervals. Consequently, observation-vector errors in different windows are temporally correlated, and the complete observation covariance $P_{y,r}$ is generally a high-dimensional dense matrix. By reorganizing the summation indices, this paper rewrites (38) from the window domain into a linear combination over the global discrete epochs. Regarding the discrete noise sequence at epochs $k = 1, 2, \dots, K_{\max}$,

$$\begin{aligned} \delta\boldsymbol{\theta}_r &= \Phi \sum_{i=1}^N (J_{\beta,i} \delta\beta_{v,i} + J_{\alpha,i} \delta\boldsymbol{\alpha}_{a,i} + J_{\alpha,i} \delta\boldsymbol{\alpha}_{g,i}) \\ &= \Phi \sum_{k=1}^{K_{\max}} (\mathcal{X}_k \mathbf{w}_{a,k} + \mathcal{Y}_k \mathbf{w}_{g,k} + \mathcal{Z}_k \mathbf{w}_{v,k}). \end{aligned} \quad (41)$$

Here $\mathbf{w}_{a,k}$, $\mathbf{w}_{g,k}$, and $\mathbf{w}_{v,k}$ are the accelerometer white noise, gyroscope white noise, and GNSS velocity white noise at epoch k , respectively. The matrices \mathcal{X}_k , \mathcal{Y}_k , and \mathcal{Z}_k are the global propagation coefficients from the corresponding noise sources to $\text{vec}(K)$. Using overlapping specific-force integrals, body-attitude propagation, and shared sliding-window endpoints, these coefficients can be written as

$$\mathcal{X}_k = \sum_{i \in \Omega_k} J_{\alpha,i} C_{b(t_k)}^{b(0)} T, \quad (42)$$

$$\mathcal{Y}_k = \sum_{i=1}^N J_{\alpha,i} \sum_{j=\max(m_i,k)}^{M_i-1} \left(-C_{b(t_j)}^{b(0)} \left[\mathbf{f}^b(t_j) \times \right] C_{b(t_k)}^{b(t_j)} T^2 \right). \quad (43)$$

$$\mathcal{Z}_k = \sum_{i \in \Omega_k^{\text{end}}} J_{\beta,i} C_{n(t_k)}^{n(0)} - \sum_{i \in \Omega_k^{\text{start}}} J_{\beta,i} C_{n(t_k)}^{n(0)}. \quad (44)$$

TABLE I
ALGORITHM FOR SLIDING-WINDOW OBA ATTITUDE ERROR EVALUATION

Stage	Operation / Computation
Initialization	Set deterministic errors ϵ^b , ∇^b , and \mathbf{l}^b ; set discrete noise covariance matrices $Q_{a,k}$, $Q_{g,k}$, and $R_{v,k}$; set total epochs K_{\max} , window count N , and sliding-window indices (m_i, M_i) .
Step 1	Propagate nominal attitude matrices $C_{b(t_k)}^{b(0)}$ and $C_{n(t_k)}^{n(0)}$; construct nominal observation pairs α_i and β_i using (12) and (13).
Step 2	Form B , Z , and the Davenport gain matrix K using (15) and (16); solve for the largest eigenvalue λ_1 and its unit eigenvector q_1 .
Step 3	Compute the core sensitivity matrix Φ from Davenport matrix perturbation to attitude error using (32).
Step 4	Compute $J_{\beta,i}$ and $J_{\alpha,i}$ for each sliding window and assemble \mathcal{J}_K using (36) and (37); the explicit Jacobian forms are given in Appendix A.
Step 5	Evaluate deterministic observation-vector errors $\delta\alpha_{g,i}$, $\delta\alpha_{a,i}$, and $\delta\alpha_{l,i}$; compute the deterministic attitude offset $\delta\theta_s$ using (40).
Step 6	Reorganize stochastic propagation by global epoch; compute \mathcal{X}_k , \mathcal{Y}_k , and \mathcal{Z}_k using (42)–(44); compute $P_{\theta,r}$ using (45).
Step 7	Output the initial attitude error statistics $E[\delta\theta] = \delta\theta_s$ and $\text{Cov}(\delta\theta) = P_{\theta,r}$ using (46); optionally obtain 3σ bounds from $\delta\theta_s \pm 3\sqrt{\text{diag}(P_{\theta,r})}$.

In (42)–(44), $\Omega_k = \{i \mid m_i \leq k \leq M_i - 1\}$ represents the set of active windows covering the k th specific-force integration epoch. Correspondingly, $\Omega_k^{\text{end}} = \{i \mid M_i = k\}$ and $\Omega_k^{\text{start}} = \{i \mid m_i = k\}$ denote the sets of windows terminating and initiating at epoch t_k , respectively. If the lower bound of the inner summation in (43) exceeds the upper bound, the term is zero. The lower bound $j = \max(m_i, k)$ in (43) arises because the gyroscope white noise at epoch k only affects past attitude propagation for subsequent epochs $j \geq k$. Equation (42) accounts for the cross-covariance introduced by sharing identical accelerometer noise samples across overlapping windows. Equation (43) preserves the influence of gyroscope noise through past body-attitude error propagation. Equation (44) merges sensitivities when the same velocity epoch is used by several windows.

Since the white-noise samples at different discrete epochs are mutually independent, cross-epoch terms vanish in $P_{\theta,r} = E[\delta\theta_r \delta\theta_r^T]$. The attitude error covariance is assembled from single-epoch variances as

$$P_{\theta,r} = \Phi \left[\sum_{k=1}^{K_{\max}} (\mathcal{X}_k Q_{a,k} \mathcal{X}_k^T + \mathcal{Y}_k Q_{g,k} \mathcal{Y}_k^T + \mathcal{Z}_k R_{v,k} \mathcal{Z}_k^T) \right] \Phi^T. \quad (45)$$

Here $Q_{a,k}$, $Q_{g,k}$, and $R_{v,k}$ are the corresponding discrete accelerometer, gyroscope, and aiding-velocity noise covariance matrices. The attitude error evaluation of sliding-window OBA is then

$$E[\delta\theta] = \delta\theta_s, \quad \text{Cov}(\delta\theta) = P_{\theta,r}. \quad (46)$$

Equation (46) indicates that systematic errors dictate the deterministic attitude offset, while stochastic noise determines the statistical envelope around it. The 3σ bounds in pitch, roll, and heading can be obtained from $\delta\theta_s \pm 3\sqrt{\text{diag}(P_{\theta,r})}$.

To facilitate practical implementation of the proposed error propagation model, the complete computational procedure for evaluating the sliding-window OBA attitude error statistics, from nominal observation construction to the final deterministic offset and covariance extraction, is summarized in Table I.

TABLE II
SIMULATION SETTINGS AND INJECTED ERROR PARAMETERS

Parameter	Value
Sampling rate f_s	100 Hz
Simulation duration T_{sim}	600 s
Window length T_w	10 s
Monte Carlo trials N_{MC}	500
Gyroscope bias ϵ^b	[0.5, -0.4, 0.3] deg/h
Accelerometer bias ∇^b	[300, -200, 250] μg
Lever arm \mathbf{l}^b	[0.8, -0.5, 0.3] m
GNSS velocity noise w_v	0.1 m/s
Gyroscope angle random walk (ARW)	0.06 deg/ $\sqrt{\text{h}}$
Accelerometer velocity random walk (VRW)	0.012 m/s/ $\sqrt{\text{h}}$

IV. SIMULATION VALIDATION

To validate the deterministic error offset and attitude error covariance models, a sliding-window OBA error-propagation simulation is designed. Two contrasting trajectories are evaluated to comprehensively test the models under varying degrees of observability and observation-vector geometry. As shown in Fig. 1, the straight trajectory represents weakly excited, low-dynamic motion, where the directions of the specific-force and velocity vectors vary slowly, rendering heading poorly observable. This scenario is used to evaluate how deterministic errors and stochastic noise are amplified under unfavorable geometry. Conversely, the Figure-8 trajectory represents strongly excited multi-axis maneuvering, where acceleration, deceleration, and turning diversify the spatial distribution of observation vectors. It is used to verify the proposed models' capability to capture the reduction in deterministic heading offsets and the accelerated convergence of the error covariance under improved observation geometry with identical error inputs. The main simulation settings are listed in Table II.

The inertial-sensor random-walk coefficients in Table II are converted to the equivalent discrete white-noise terms w_g and w_a in (18) at $f_s = 100$ Hz, i.e., $\Delta t = 0.01$ s. Accordingly, the discrete samples are modeled as $w_{g,k} \sim \mathcal{N}(\mathbf{0}, (0.01 \text{ deg/s})^2 I_3)$ and $w_{a,k} \sim \mathcal{N}(\mathbf{0}, (0.002 \text{ m/s}^2)^2 I_3)$, where $0.01 = (0.06/60)/\sqrt{\Delta t}$ and $0.002 = (0.012/60)/\sqrt{\Delta t}$.

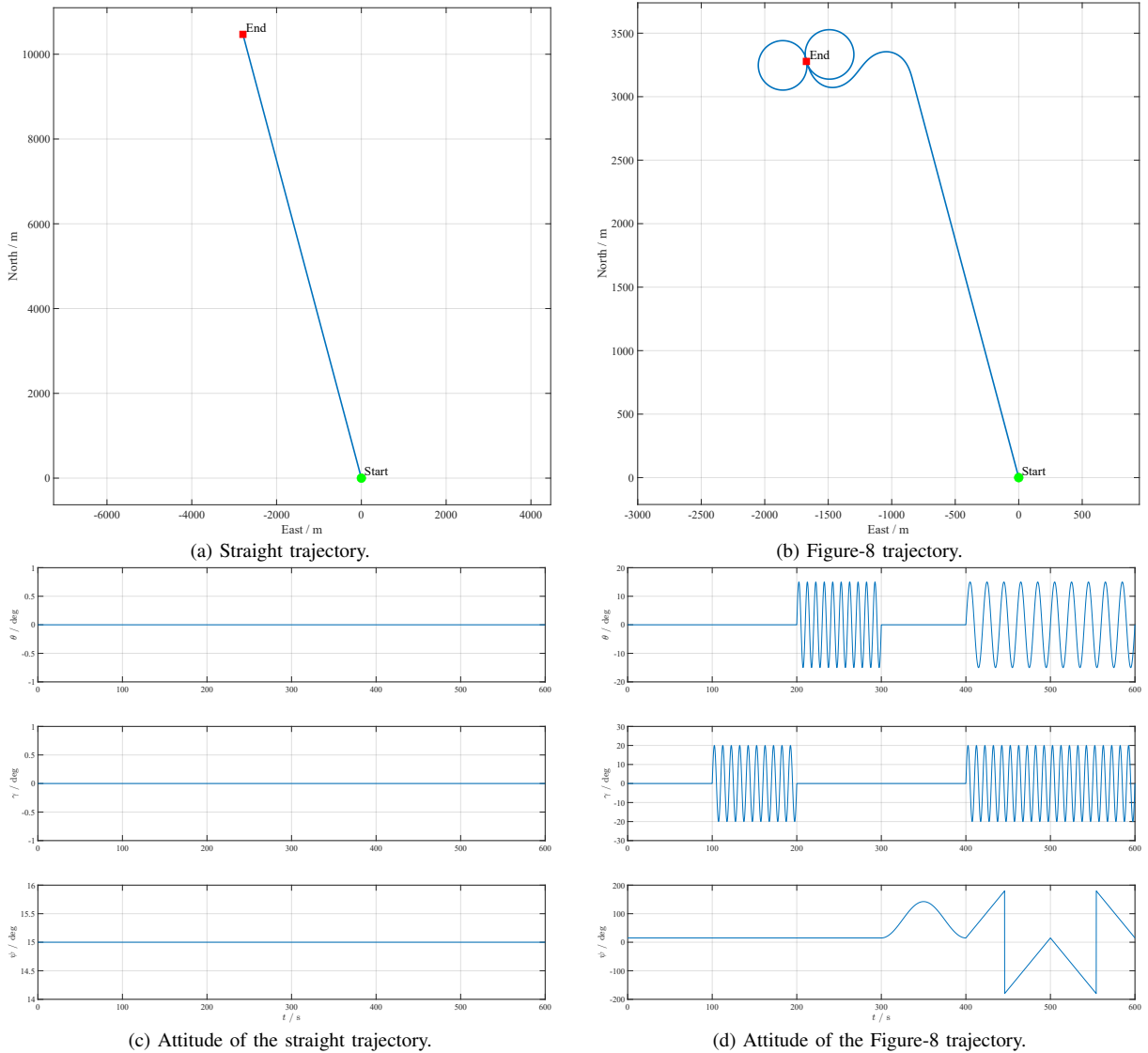


Fig. 1. Straight and Figure-8 trajectories and their corresponding attitude profiles, designed to compare weakly and strongly excited motion conditions.

The simulation is organized into three complementary parts. First, deterministic error sources ϵ^b , ∇^b , and l^b are injected individually and jointly to examine the predicted deterministic attitude offset. Second, stochastic error sources w_g , w_a , and w_v are injected individually and jointly, and the Monte Carlo standard deviations are compared with the covariance prediction. Third, all deterministic and stochastic error sources are injected simultaneously to examine whether the predicted deterministic offset and the $\pm 3\sigma$ envelope jointly characterize and bound the OBA initial-attitude error. All Monte Carlo simulations utilize 500 trials to derive the detailed statistical results presented below.

A. Deterministic Error

The deterministic experiment compares the OBA initial-attitude error obtained after injecting deterministic error sources with the first-order analytical prediction in (40). To quantify this comparison, the three-axis discrepancy between the numerical OBA result and the analytical prediction is

herein defined as the prediction residual. This residual is evaluated using two metrics: the Euclidean norm at the final epoch and the overall root-mean-square error (RMSE) across the entire time series. Table III summarizes these prediction residuals under individual and joint error injections, while Fig. 2 illustrates the time-domain evolution of the deterministic attitude offsets under the simultaneous injection of all deterministic error sources. The inset in each subplot displays the instantaneous residual, revealing the micro-level discrepancies between the two nearly overlapping curves.

The nearly overlapping analytical and numerical attitude error curves in Fig. 2 show that the first-order analytical model accurately predicts the dominant deterministic offsets induced by sensor biases and lever arms. The attitude errors differ significantly in magnitude and convergence rate: horizontal attitude errors converge rapidly to the order of 10^{-2} – 10^{-3} deg, whereas heading errors are significantly larger and converge more slowly. This slow heading convergence is particularly pronounced under the straight trajectory; under low excita-

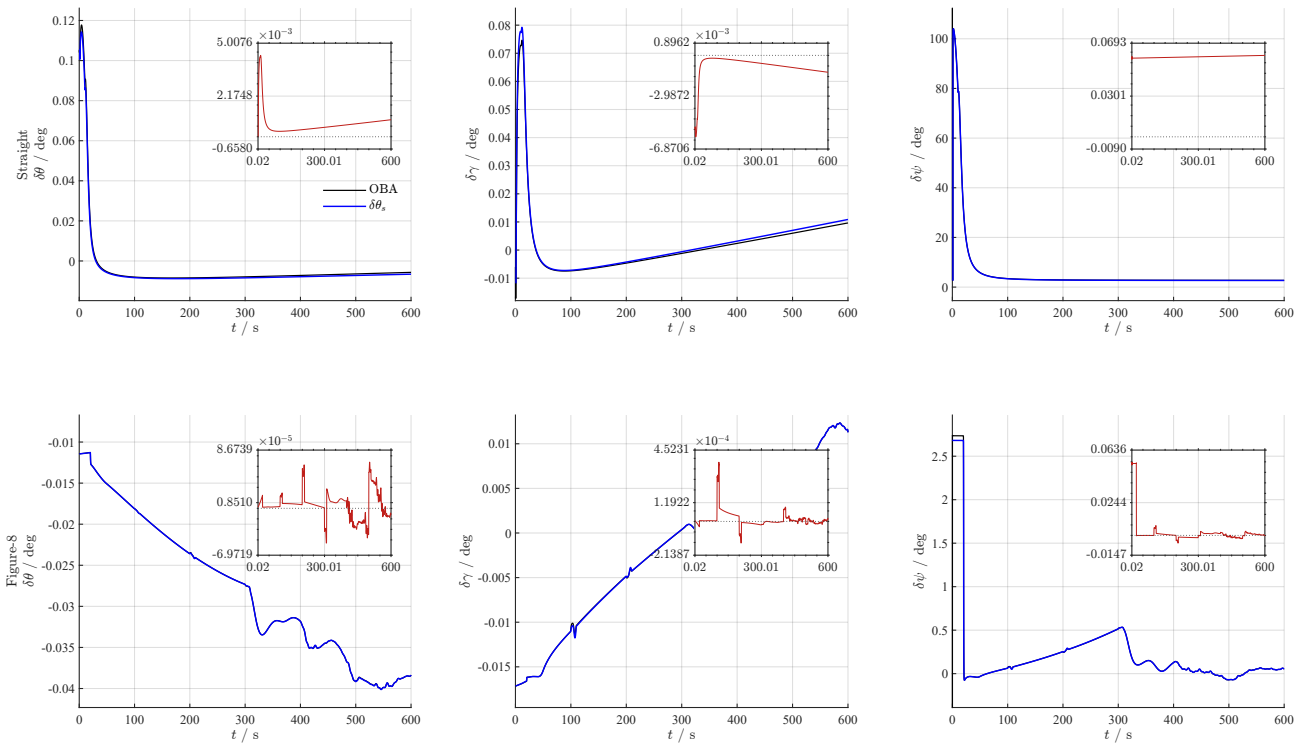


Fig. 2. OBA initial-attitude error and first-order analytical prediction under the joint injection of ϵ^b , ∇^b , and l^b for the straight and Figure-8 trajectories.

TABLE III
DETERMINISTIC INITIAL-ATTITUDE PREDICTION RESIDUAL NORMS

Trajectory	Source	Final residual norm / deg	Residual RMSE / deg
Straight	ϵ^b	6.132×10^{-2}	6.027×10^{-2}
Straight	∇^b	6.567×10^{-6}	4.390×10^{-5}
Straight	l^b	2.289×10^{-7}	2.477×10^{-5}
Straight	$\epsilon^b + \nabla^b + l^b$	6.029×10^{-2}	5.927×10^{-2}
Figure-8	ϵ^b	6.888×10^{-5}	1.001×10^{-2}
Figure-8	∇^b	8.200×10^{-6}	8.651×10^{-5}
Figure-8	l^b	3.815×10^{-4}	1.658×10^{-3}
Figure-8	$\epsilon^b + \nabla^b + l^b$	4.352×10^{-4}	9.940×10^{-3}

tion, the vertical gyroscope bias becomes weakly observable, causing the converged initial attitude to exhibit a fixed heading offset exceeding 2.5 deg in the joint deterministic case, which will induce cumulative errors in the current-epoch attitude through the matrix chain multiplication in (2). In contrast, the Figure-8 maneuver improves the observation geometry and suppresses this deterministic heading offset to below 0.1 deg.

Beyond these macroscopic attitude offsets, the red curves in the insets of Fig. 2 illustrate the time-domain evolution of the prediction residuals between the analytical and numerical results. The magnitudes of these prediction residuals are orders of magnitude smaller than the corresponding attitude offsets, confirming that the analytical model accurately captures the evolution trends of the attitude errors. As quantitatively detailed in Table III, under the straight trajectory where the heading is weakly observable, the gyroscope bias serves as the primary source of the prediction residuals. Its contribution (6.132×10^{-2} deg) is significantly higher than those of the

accelerometer bias (6.567×10^{-6} deg) and the lever-arm effect (2.289×10^{-7} deg). In contrast, under the Figure-8 maneuver, the improved observation geometry effectively mitigates the gyroscope-induced errors, reducing its residual to 6.888×10^{-5} deg, while the associated angular motion excites the lever-arm effect, causing it to emerge as the dominant contributor to the prediction residuals (3.815×10^{-4} deg). Notably, under the straight trajectory with joint error injection, the final Euclidean norm of the prediction residual (6.029×10^{-2} deg) slightly exceeds its overall RMSE (5.927×10^{-2} deg). Corroborated by the inset curves in Fig. 2, this phenomenon arises because the weakly observable gyroscope bias induces a slow accumulation trend in the prediction residual, driving the terminal value slightly above the overall average level.

B. Attitude Error Covariance

To validate the stochastic error propagation, the covariance experiment separately and jointly injects the random noise sources w_g , w_a , and w_v . The performance is evaluated using the standard-deviation ratio $\hat{\sigma}_{MC}/\sigma_{pred}$ for each attitude axis, where a ratio near unity indicates a precise match between the empirical Monte Carlo dispersion and the analytical covariance prediction derived in (45).

As depicted by the heatmaps in Fig. 3, the analytical covariance model accurately captures the impact of varying observation geometries, maintaining all three-axis attitude-error standard-deviation ratios strictly between 0.929 and 1.060 across both trajectories. Specifically, under the straight trajectory, the heading is highly susceptible to measurement noise due to weak observability. Although this leads to significantly amplified heading variance, the standard-deviation

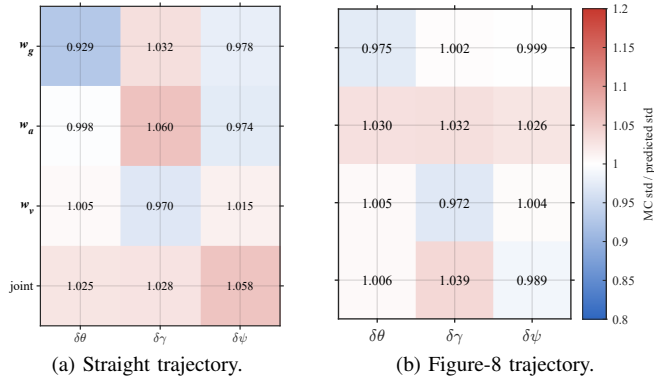


Fig. 3. Standard-deviation ratio heatmaps for the straight and Figure-8 trajectories.

ratios in Fig. 3(a) remain close to unity. For instance, the ratio for the heading angle under joint noise injection is 1.058, confirming that the analytical model precisely predicts this amplification. In contrast, the Figure-8 maneuver improves the observation geometry and effectively reduces the actual heading uncertainty; correspondingly, the heading standard-deviation ratio, defined as the proportion of Monte Carlo samples falling within the $\pm 3\sigma$ envelope, quantifies the overall reliability of the statistical boundaries. Finally, the standard-deviation ratio assesses the tightness of the analytical covariance, examining whether the predicted statistical bounds are overly conservative.

TABLE IV
STATISTICAL SUMMARY UNDER SIMULTANEOUS ERROR INJECTION

Trajectory Axis		Final mean residual / deg	Std. ratio	Coverage
Straight	Pitch	8.99×10^{-4}	1.036	0.994
Straight	Roll	-7.65×10^{-5}	0.944	0.998
Straight	Heading	6.75×10^{-2}	0.998	0.996
Figure-8	Pitch	-1.94×10^{-4}	1.018	0.998
Figure-8	Roll	1.27×10^{-3}	0.942	0.998
Figure-8	Heading	9.23×10^{-4}	1.017	0.996

C. Combined-Error Envelope

To comprehensively evaluate the complete error propagation model, the final simulation simultaneously injects all deterministic and stochastic error sources. Under the simultaneous injection of all errors, the deterministic model dictates the time-varying attitude offset $\delta\theta_s$, while the covariance model establishes the dynamic statistical bounds, i.e., the $\pm 3\sigma$ envelope. The final mean residual in Table IV is defined as the difference between the 500-trial Monte Carlo average of the final OBA initial-attitude errors and the analytically predicted deterministic offset, serving to evaluate the accuracy of the attitude offset. Subsequently, the empirical coverage ratio, quantifies the overall reliability of the statistical boundaries. Finally, the standard-deviation ratio assesses the tightness of the analytical covariance, examining whether the predicted statistical bounds are overly conservative.

As illustrated in Fig. 4, the analytical $\pm 3\sigma$ envelopes

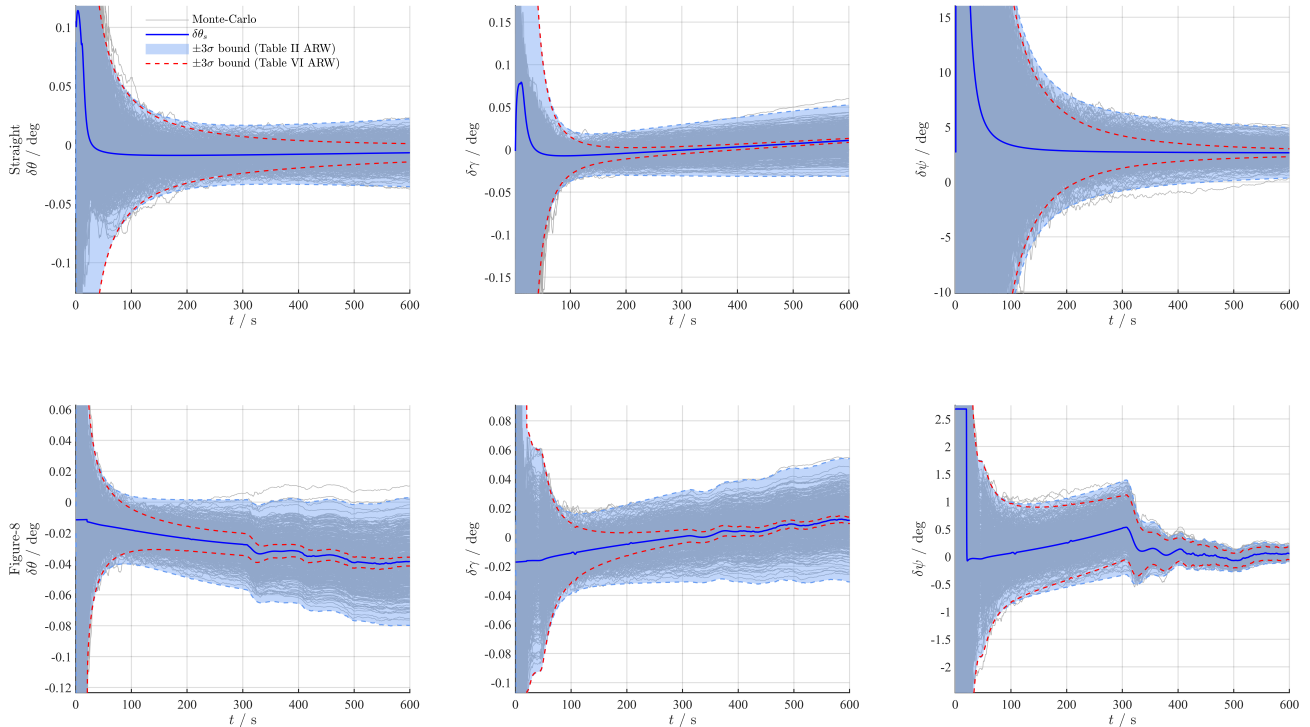


Fig. 4. Monte Carlo OBA initial-attitude errors and analytical $\pm 3\sigma$ envelopes under the simultaneous injection of all error sources for the straight and Figure-8 trajectories. The blue and red dashed lines represent the analytical bounds evaluated with the ARW parameters from Table II and the NS260 sensor (Table VI), respectively.

effectively bound the 500-trial Monte Carlo error trajectories. The results in Table IV confirm this conclusion: the empirical coverage ratios reliably achieve 0.994–0.998, while the combined-error standard-deviation ratios ranging from 0.942 to 1.036 show that these boundaries are both tight and precise. Furthermore, the mean prediction residuals remain on the order of 10^{-5} to 10^{-2} deg, confirming that the analytical model accurately captures the deterministic attitude offsets under coupled deterministic and stochastic errors. A comparison of the heading responses in Fig. 4 further reveals that the turning maneuver starting near $t = 300$ s significantly improves the observation geometry, thereby accelerating the convergence of the heading error. These results demonstrate that the proposed first-order model characterizes the total OBA initial-attitude error without degradation under the simultaneous coupling of multiple error sources.

It is noteworthy in Fig. 4 that the horizontal covariance envelopes (blue dashed lines) initially converge rapidly but subsequently exhibit a slight expansion trend. The fundamental cause of this phenomenon lies in the magnitude of the gyroscope ARW and its coupling effect with the specific force. According to the stochastic propagation coefficient \mathcal{Y}_k in (43), the gyroscope noise is projected into the attitude error covariance $P_{\theta,r}$ via the cross-product matrix $[\mathbf{f}^b(t_j) \times]$. Because gravity strictly dominates the specific force \mathbf{f}^b , this cross-product operation causes the horizontal components of the observation-vector error $\delta\alpha_g$ to be significantly larger than the vertical counterpart. As the alignment duration extends, the severe degradation of these late-stage α_i vectors eventually outweighs the statistical benefit of accumulating more observation pairs, leading to the late-stage inflation of the horizontal attitude covariance. In contrast, the heading error covariance primarily couples with the much smaller horizontal specific forces, thereby avoiding this gravity-amplified covariance inflation. To explicitly substantiate this mechanism, the analytical bounds are replotted (red dashed lines) using the actual ARW of the high-precision fiber-optic gyroscope utilized in the vehicle field test. As shown in Fig. 4, with the ARW drastically reduced from the Table II value $0.06^\circ/\sqrt{\text{h}}$ to the maximum NS260 value $1.864 \times 10^{-3} \text{ }^\circ/\sqrt{\text{h}}$ in Table VI, the horizontal covariance envelopes exhibit a monotonically converging trend within the 600 s alignment duration, as the critical point of divergence is substantially delayed.

V. VEHICLE FIELD-TEST VALIDATION

To evaluate whether the proposed error-propagation model remains valid with real sensor data, a vehicle field test was conducted using two rigidly mounted navigation systems, as shown in Fig. 5. The FSINS3X/RTK combination provides the ground truth: its integrated attitude, velocity, and position outputs serve as the reference baseline for evaluating the OBA initial-attitude errors. The NS260 with single-point GNSS provides the test data: its raw inertial measurements and GNSS velocity are processed by the sliding-window OBA algorithm, and the resulting initial attitude is compared with the reference baseline to calculate the actual initial-attitude estimation error. Table V details the specifications and configurations of both

systems. Consequently, the primary objective of this field test is to directly verify whether the analytical attitude offsets and covariance envelopes accurately capture the actual initial-attitude errors generated by the test system.

To verify the analytical error-propagation mechanism, approximately 3200 s of FSINS3X/RTK reference solutions and NS260/GNSS raw data were continuously recorded during the field test, as shown in Fig. 6. From this overall dataset, a 600 s dynamic segment and a 600 s static segment were specifically extracted to process the raw measurements via the sliding-window velocity-integration OBA. Featuring drastic velocity variations and intense attitude maneuvers, the dynamic segment yields a well-conditioned observation geometry that enables reliable estimation of deterministic errors, including sensor biases and the lever arm. Conversely, the nearly motionless static segment degrades heading observability, serving as a stringent evaluation to verify whether the analytical covariance model correctly predicts the amplification of the heading error envelope under poor excitation.

The primary objective of this vehicle field test is to verify whether the proposed analytical error-propagation equations correctly model the actual OBA initial-attitude errors. Consequently, to rigorously validate the analytical model, its input parameters detailed in Table VI must accurately reflect the true hardware characteristics. These parameters are extracted through offline calibration using raw data, rather than relying on generic manufacturer nominal values or rough artificial estimates, thereby minimizing prediction residuals induced by mismatched input parameters. For practical online deployment, appropriately enlarged empirical nominal values or online estimates could also be adopted as inputs so that the analytical model still outputs a conservative error bound. Specifically, the gyroscope ARW and accelerometer VRW coefficients are extracted via Allan-variance analysis using approximately 5 h of static IMU raw data, while the GNSS velocity noise is configured based on the performance specifications of the UM982 GNSS receiver.

To obtain the deterministic error parameters, a classical 18-state SINS/GNSS Kalman filter, utilizing a six-dimensional position and velocity measurement vector and initialized by the reference baseline, is executed on the 600 s dynamic segment. Since both the static and dynamic segments are extracted from the same continuous vehicle test, their deterministic errors, i.e., turn-on biases and mechanically fixed lever arm, remain strictly identical. Aided by the strong observability of the dynamic maneuvers, the filter yields highly reliable steady-state estimates for these parameters. As illustrated in Fig. 7, these converged steady-state values are extracted to serve as constant inputs across both static and dynamic OBA evaluations.

After the NS260 OBA initial attitude is obtained, the actual initial-attitude error is computed by subtracting the FSINS3X/RTK reference baseline. Because the reference and test systems are installed independently, a fixed mounting angle exists between the two systems. To eliminate the attitude deviation induced by this fixed mounting angle, the mean difference between the integrated attitude outputs of both systems over the final 100 s static period of the entire

TABLE V
HARDWARE CONFIGURATION AND SYSTEM SPECIFICATIONS

System role	Configuration	Integrated accuracy	Output rate
Reference baseline	FSINS3X + RTK	Pitch/Roll/Heading: $0.02^\circ/0.02^\circ/0.06^\circ$ Velocity: 0.03 m/s Position: 5 cm (horizontal), 10 cm (vertical)	200 Hz
Test system	NS260 + single-point GNSS	Error parameters detailed in Table VI.	200 Hz

TABLE VI
INPUT PARAMETERS FOR THE NS260 ANALYTICAL ERROR MODEL

Parameter	Value
Sampling rate f_s	200 Hz
Simulation duration T_{sim}	600 s
Window length T_w	10 s
Gyroscope bias ϵ^b	$[0.1879, 0.3488, -0.1057]$ deg/h
Accelerometer bias ∇^b	$[61.7, -1496.0, -580.8]$ μg
Lever arm l^b	$[0.8041, -0.5724, 0.0494]$ m
GNSS velocity noise w_v	$[0.10, 0.10, 0.10]$ m/s
Gyroscope angle random walk (ARW)	$[1.856, 1.864, 0.685] \times 10^{-3}$ deg/ \sqrt{h}
Accelerometer velocity random walk (VRW)	$[0.00882, 0.00644, 0.00947]$ m/s/ \sqrt{h}

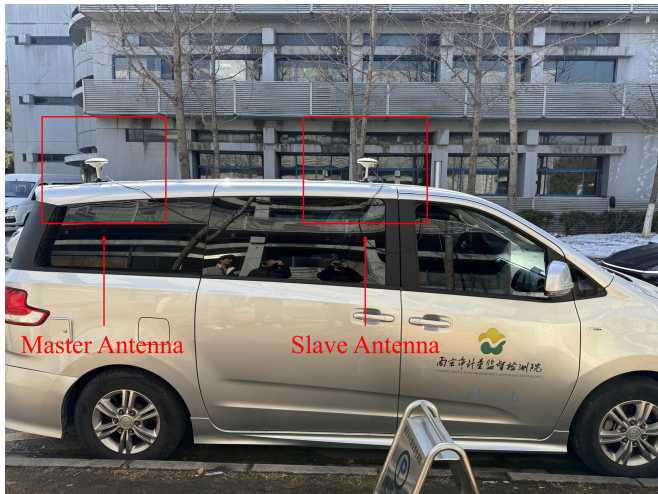
3200 s field test is extracted as the global mounting angle and subsequently subtracted. This calibration aligns only the physical reference frames; it does not alter the transient error evolution or the statistical spread predicted by the proposed model. For Table VII, the single-axis final residual is the difference between the actual initial-attitude error and the predicted deterministic offset at the final epoch. The steady-state RMSE is computed from the prediction residual over the final 10 s of each test segment, while the empirical coverage ratio is evaluated over the entire segment duration.

Building upon this calibration, Fig. 8 compares the actual NS260 initial-attitude errors against the predicted deterministic offset and analytical $\pm 3\sigma$ envelope to validate the proposed

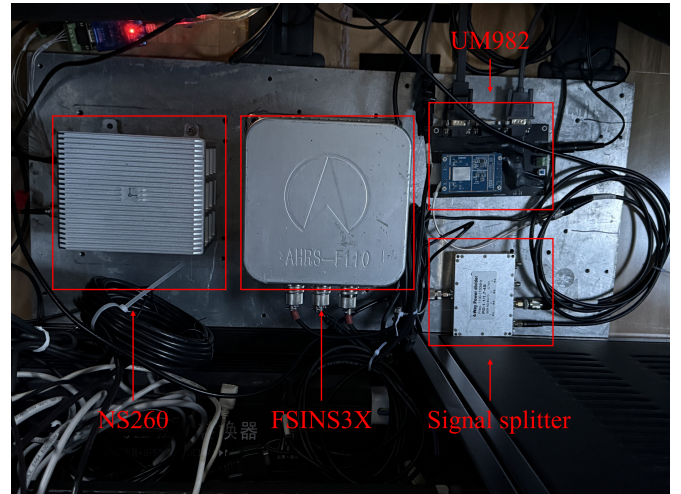
TABLE VII
STATISTICAL SUMMARY OF PREDICTION RESIDUALS IN THE NS260 FIELD TEST

Segment	Axis	Final residual / deg	Steady-state RMSE / deg	Coverage
Static	Pitch	0.00054	0.00031	0.999
Static	Roll	0.00024	0.00014	1.000
Static	Heading	-0.00526	0.00378	0.999
Dynamic	Pitch	-0.00038	0.00046	0.941
Dynamic	Roll	-0.00031	0.00018	0.998
Dynamic	Heading	0.01486	0.00495	0.989

model under both static and dynamic conditions. In the static segment, Fig. 8 shows that the heading envelope is significantly wider than those of pitch and roll. This aligns with the weak heading observability inherent to stationary conditions, where the velocity-integration-based observation vectors lack kinematic excitation. Despite this unfavorable condition, Table VII demonstrates that the coverage ratios remain 0.999, 1.000, and 0.999 for static pitch, roll, and heading, respectively, while the maximum steady-state RMSE is only 0.00378 deg in heading. In the dynamic segment, the continuous vehicle maneuvers enhance the system observability; consequently, Fig. 8 illustrates a rapid convergence of the heading error covariance over time. Quantitatively, Table VII indicates that the final prediction residuals for the dynamic segment are bounded within 0.01486 deg, with steady-state RMSEs strictly below 0.00495 deg. The coverage ratios reach 0.941, 0.998, and 0.989 for dynamic pitch, roll, and heading, respectively.

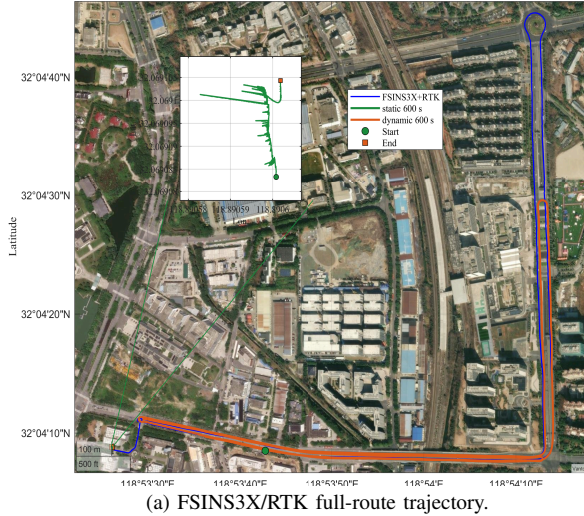


(a) Dual-antenna vehicle platform.

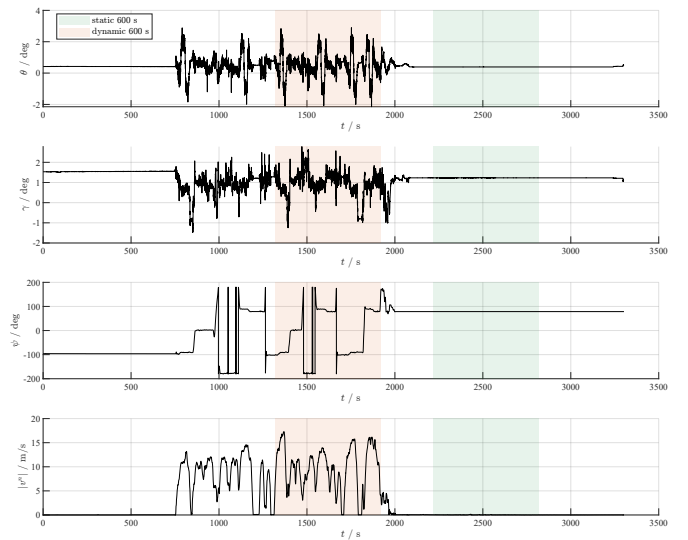


(b) Onboard INS/GNSS installation.

Fig. 5. Vehicle platform and onboard installation of the NS260 experimental unit and the FSINS3X/RTK reference system.



(a) FSINS3X/RTK full-route trajectory.



(b) Reference attitude and velocity profiles.

Fig. 6. Reference trajectory and motion profiles used in the vehicle field test. The trajectory map marks the route start/end points and features a magnified inset detailing the small-scale positional fluctuations during the static segment, while the attitude and velocity profiles show the selected static and dynamic 600 s intervals.

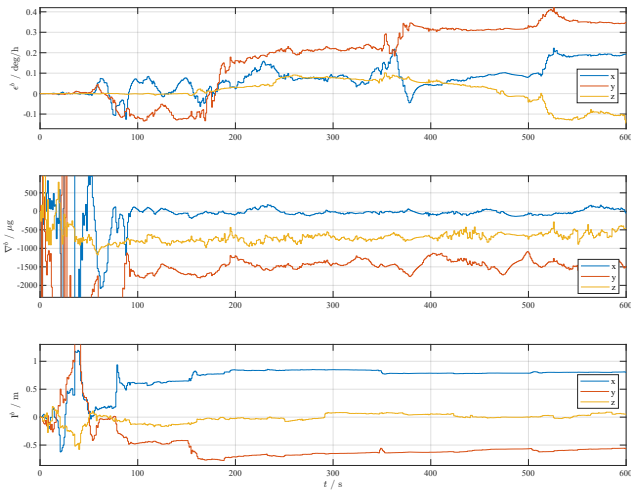


Fig. 7. Convergence histories of the SINS/GNSS Kalman filter during the dynamic segment, which are used to extract the deterministic error inputs for the NS260 test system.

Ultimately, the observed error-evolution behaviors in Fig. 8 and the rigorous statistical metrics in Table VII jointly verify that the proposed first-order model accurately predicts both the deterministic offset and the stochastic envelope under real-world vehicle testing.

VI. CONCLUSION

This paper develops a first-order analytical propagation model from nominal sliding-window observation construction to raw sensor error propagation and Davenport-based attitude error evaluation for coarse alignment based on GNSS-aided sliding-window velocity-integral OBA. Under the ENU/RFU convention, the continuous observation model, dual-sample discrete implementation, and Wahba-Davenport attitude solution are formulated, and the equivalence between the largest-

eigenvalue solution of the Davenport gain matrix and the smallest-eigenvalue solution of the OBA homogeneous residual matrix is clarified.

Gyroscope errors, accelerometer errors, GNSS velocity errors, and GNSS lever-arm effects are incorporated into a unified observation-vector error model. Accelerometer error directly enters the α -side specific-force integral, gyroscope error enters the same side through accumulated attitude projection, GNSS velocity error mainly enters the β side through sliding-window endpoint differencing, and the uncompensated lever-arm effect can be equivalently moved to an α -side endpoint term. Based on the resulting observation-vector error equations, a linear propagation relation from observation-vector perturbation to Davenport matrix perturbation and then to three-dimensional attitude error is established.

The deterministic and stochastic components jointly quantify sliding-window OBA coarse-alignment accuracy. The deterministic component predicts the attitude offsets caused by gyroscope bias, accelerometer bias, and lever-arm uncertainty, whereas the stochastic component predicts the attitude error covariance caused by GNSS velocity noise, accelerometer noise, and gyroscope noise. Simulation results demonstrate that the analytically predicted deterministic offsets are consistent with the numerical OBA results, the 500-trial Monte Carlo standard deviations are highly consistent with the predicted analytical covariances, and the combined-error empirical coverage ratios remain within 0.994–0.998. The vehicle field test further shows that, after global mounting angle compensation, the NS260 OBA initial-attitude errors remain bounded within the predicted deterministic offsets and the $\pm 3\sigma$ envelopes, with steady-state RMSE below 0.00495 deg and a maximum final residual of 0.01486 deg. These results indicate that the first-order covariance model characterizes the true statistical dispersion without obvious accuracy degradation due to the truncation of higher-order terms. Consequently, the proposed

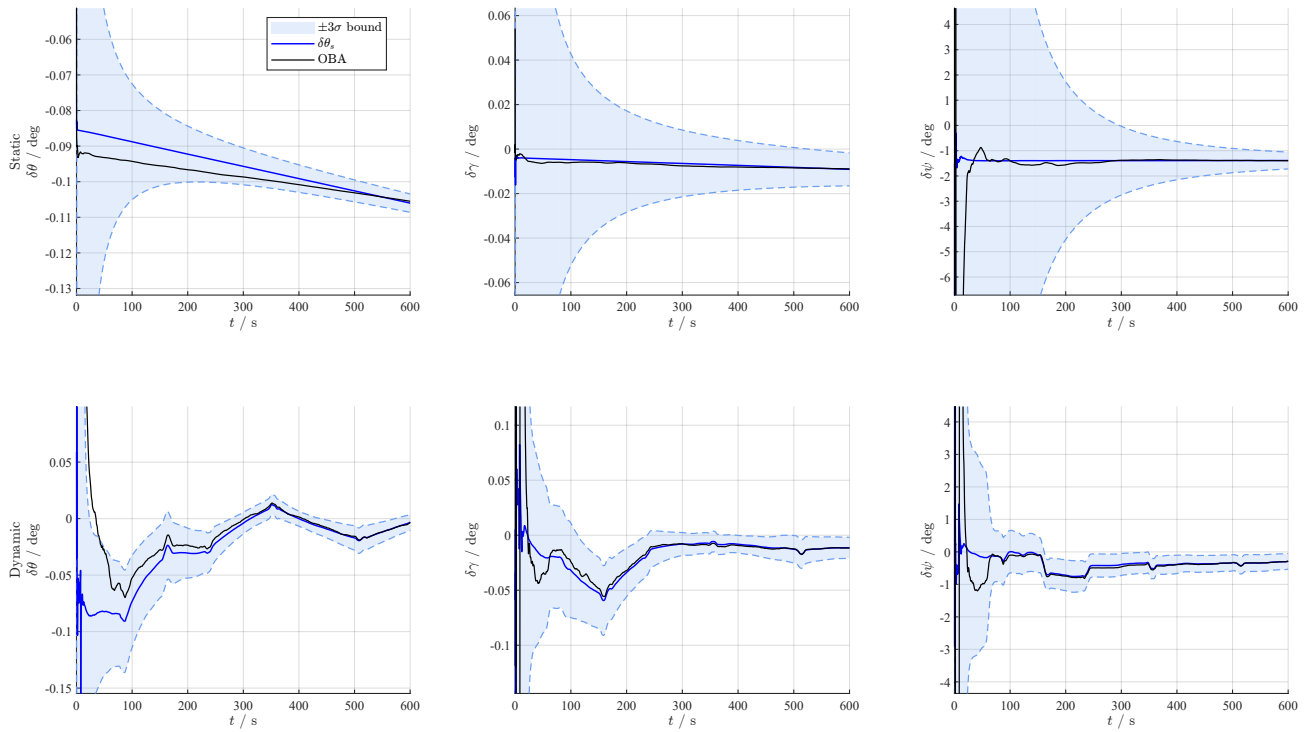


Fig. 8. Comparison of the actual OBA initial-attitude errors with the analytically predicted offset and $\pm 3\sigma$ envelopes for the NS260 field test over the static and dynamic segments.

model can serve as an attitude accuracy evaluation metric for GNSS-aided sliding-window OBA coarse alignment.

It should be noted that the proposed model rigorously evaluates the estimation error of the constant initial attitude matrix $C_b^n(0)$. The real-time attitude error at the end of the alignment process, which further incorporates the continuously accumulating gyroscope integration errors over the interval $[0, t]$, is not directly accounted for in this first-order mapping. Extending the current framework to completely map observation-vector perturbations to the real-time attitude error covariance remains a valuable direction for future research.

APPENDIX A

DERIVATION OF THE OBSERVATION-VECTOR JACOBIANS

This appendix gives the explicit forms of the Jacobian matrices in (36). Because the present derivation uses the Davenport gain matrix K in the maximization form of (17), the Jacobians differ from those obtained from the homogeneous residual matrix K_{OBA} . Directly applying the residual-matrix derivatives would introduce a factor of -2 and an additional diagonal shift induced by the perturbation of cI_4 in $K_{\text{OBA}} = cI_4 - 2K$.

For one observation pair, let

$$\beta_i = [v_1, v_2, v_3]^T, \quad \alpha_i = [u_1, u_2, u_3]^T. \quad (47)$$

Using $\text{tr}(ab^T) = b^T a$, the first-order perturbations entering K are

$$\delta B_i = w_i (\delta \beta_i \alpha_i^T + \beta_i \delta \alpha_i^T), \quad (48)$$

$$\text{tr}(\delta B_i) = w_i (\alpha_i^T \delta \beta_i + \beta_i^T \delta \alpha_i), \quad (49)$$

$$\delta Z_i = w_i (\delta \beta_i \times \alpha_i + \beta_i \times \delta \alpha_i). \quad (50)$$

Substitution of (48)–(50) into (35) and column-wise vectorization give

$$\text{vec}(\delta K_i) = J_{\beta,i} \delta \beta_i + J_{\alpha,i} \delta \alpha_i, \quad (51)$$

where $J_{\beta,i}, J_{\alpha,i} \in \mathbb{R}^{16 \times 3}$ are obtained by differentiating each element of $\text{vec}(K)$ with respect to the components of β_i and α_i . Under the column-major ordering used by $\text{vec}(\cdot)$,

$$J_{\beta,i} = w_i \begin{bmatrix} u_1 & u_2 & u_3 \\ 0 & u_3 & -u_2 \\ -u_3 & 0 & u_1 \\ u_2 & -u_1 & 0 \\ 0 & u_3 & -u_2 \\ u_1 & -u_2 & -u_3 \\ u_2 & u_1 & 0 \\ u_3 & 0 & u_1 \\ -u_3 & 0 & u_1 \\ u_2 & u_1 & 0 \\ -u_1 & u_2 & -u_3 \\ 0 & u_3 & u_2 \\ u_2 & -u_1 & 0 \\ u_3 & 0 & u_1 \\ 0 & u_3 & u_2 \\ -u_1 & -u_2 & u_3 \end{bmatrix}, \quad (52)$$

and

$$J_{\alpha,i} = w_i \begin{bmatrix} v_1 & v_2 & v_3 \\ 0 & -v_3 & v_2 \\ v_3 & 0 & -v_1 \\ -v_2 & v_1 & 0 \\ 0 & -v_3 & v_2 \\ v_1 & -v_2 & -v_3 \\ v_2 & v_1 & 0 \\ v_3 & 0 & v_1 \\ v_3 & 0 & -v_1 \\ v_2 & v_1 & 0 \\ -v_1 & v_2 & -v_3 \\ 0 & v_3 & v_2 \\ -v_2 & v_1 & 0 \\ v_3 & 0 & v_1 \\ 0 & v_3 & v_2 \\ -v_1 & -v_2 & v_3 \end{bmatrix}. \quad (53)$$

Stacking all observation pairs yields the global Jacobian J_K in (37), and hence the complete first-order attitude error mapping in (38).

REFERENCES

- [1] P. D. Groves, *Principles of GNSS, Inertial, and Multisensor Integrated Navigation Systems*, 2nd ed. Boston, MA, USA: Artech House, 2013.
- [2] M. B. Ignagni, *Strapdown Navigation Systems: Theory and Application*. Champlain, NY, USA: Champlain Press, 2018.
- [3] B. Zhang, X. Wang, H. Lu, H. Zhaojun, and G. Changchao, "Application of adaptive robust CKF in SINS/GPS initial alignment with large azimuth misalignment angle," *Mathematical Problems in Engineering*, vol. 2021, pp. 1–13, 2021, doi: 10.1155/2021/7398706.
- [4] F. L. Markley and J. L. Crassidis, *Fundamentals of Spacecraft Attitude Determination and Control*. New York, NY, USA: Springer, 2014, doi: 10.1007/978-1-4939-0802-8.
- [5] Y. Liu, R. Yu, Z. Xiong, and Y. Guo, "Research on algorithms for multi-vector attitude determination," *Mathematical Problems in Engineering*, vol. 2022, pp. 1–12, 2022, doi: 10.1155/2022/6137308.
- [6] J. Wu, Z. Zhou, B. Gao, R. Li, Y. Cheng, and H. Fourati, "Fast linear quaternion attitude estimator using vector observations," *IEEE Transactions on Automation Science and Engineering*, vol. 15, no. 1, pp. 307–319, 2018, doi: 10.1109/TASE.2017.2699221.
- [7] T. Gaiffe, Y. Cotureau, N. Faussot, G. Hardy, P. Simonpietri, and H. Arditty, "Highly compact fiber optic gyrocompass for applications at depths up to 3000 meters," in *Proc. 2000 Int. Symp. Underwater Technology*, 2000, pp. 155–160, doi: 10.1109/UT.2000.852533.
- [8] J. C. Kinsey and L. L. Whitcomb, "Adaptive identification on the group of rigid-body rotations and its application to underwater vehicle navigation," *IEEE Transactions on Robotics*, vol. 23, no. 1, pp. 124–136, 2007, doi: 10.1109/TRO.2006.886829.
- [9] D. Gu, N. El-Sheimy, T. Hassan, and Z. Syed, "Coarse alignment for marine SINS using gravity in the inertial frame as a reference," in *Proc. IEEE/ION Position, Location and Navigation Symposium*, 2008, pp. 961–965, doi: 10.1109/PLANS.2008.4570038.
- [10] M. Wu, Y. Wu, X. Hu, and D. Hu, "Optimization-based alignment for inertial navigation systems: Theory and algorithm," *Aerospace Science and Technology*, vol. 15, no. 1, pp. 1–17, 2011, doi: 10.1016/j.ast.2010.05.004.
- [11] P. M. G. Silson, "Coarse alignment of a ship's strapdown inertial attitude reference system using velocity loci," *IEEE Transactions on Instrumentation and Measurement*, vol. 60, no. 6, pp. 1930–1941, 2011, doi: 10.1109/TIM.2011.2113131.
- [12] Y. Wu, H. Zhang, M. Wu, X. Hu, and D. Hu, "Observability of strapdown INS alignment: A global perspective," *IEEE Transactions on Aerospace and Electronic Systems*, vol. 48, no. 1, pp. 78–102, 2012, doi: 10.1109/TAES.2012.6129622.
- [13] Y. Wu and X. Pan, "Velocity/position integration formula Part I: Application to in-flight coarse alignment," *IEEE Transactions on Aerospace and Electronic Systems*, vol. 49, no. 2, pp. 1006–1023, 2013, doi: 10.1109/TAES.2013.6494395.
- [14] Y. Wu, J. Wang, and D. Hu, "A new technique for INS/GNSS attitude and parameter estimation using online optimization," *IEEE Transactions on Signal Processing*, vol. 62, no. 10, pp. 2642–2655, 2014, doi: 10.1109/TSP.2014.2312317.
- [15] L. Chang, J. Li, and K. Li, "Optimization-based alignment for strapdown inertial navigation system: Comparison and extension," *IEEE Transactions on Aerospace and Electronic Systems*, vol. 52, no. 4, pp. 1697–1713, 2016, doi: 10.1109/TAES.2016.130824.
- [16] Y. Huang, Y. Zhang, and X. Wang, "Kalman-filtering-based in-motion coarse alignment for odometer-aided SINS," *IEEE Transactions on Instrumentation and Measurement*, vol. 66, no. 12, pp. 3364–3377, 2017, doi: 10.1109/TIM.2017.2737840.
- [17] Y. Huang, Y. Zhang, and L. Chang, "A new fast in-motion coarse alignment method for GPS-aided low-cost SINS," *IEEE/ASME Transactions on Mechatronics*, vol. 23, no. 3, pp. 1303–1313, 2018, doi: 10.1109/TMECH.2018.2835486.
- [18] Y. Huang, Z. Zhang, S. Du, Y. Li, and Y. Zhang, "A high-accuracy GPS-aided coarse alignment method for MEMS-based SINS," *IEEE Transactions on Instrumentation and Measurement*, vol. 69, no. 10, pp. 7914–7932, 2020, doi: 10.1109/TIM.2020.2983578.
- [19] Z. Li, J. Wang, J. Gao, B. Li, and F. Zhou, "A Vondrak low pass filter for IMU sensor initial alignment on a disturbed base," *Sensors*, vol. 14, no. 12, pp. 23803–23821, 2014, doi: 10.3390/s141223803.
- [20] Y. Yao, X. Xu, Y. Zhu, and X. Xu, "In-motion coarse alignment method for SINS/DVL with the attitude dynamics," *ISA Transactions*, vol. 105, pp. 377–386, 2020, doi: 10.1016/j.isatra.2020.05.033.
- [21] Y. Yao, X. Xu, T. Zhang, and G. Hu, "An improved initial alignment method for SINS/GPS integration with vectors subtraction," *IEEE Sensors Journal*, vol. 21, no. 16, pp. 18256–18262, 2021, doi: 10.1109/JSEN.2021.3085742.
- [22] X. Xu, J. Gui, Y. Sun, Y. Yao, and T. Zhang, "A robust in-motion alignment method with inertial sensors and Doppler velocity log," *IEEE Transactions on Instrumentation and Measurement*, vol. 70, pp. 1–13, 2021, doi: 10.1109/TIM.2020.3011873.
- [23] X. Xu, Y. Sun, Y. Yao, and T. Zhang, "A robust in-motion optimization-based alignment for SINS/GPS integration," *IEEE Transactions on Intelligent Transportation Systems*, vol. 23, no. 5, pp. 4362–4372, 2022, doi: 10.1109/TITS.2020.3044084.
- [24] X. Xu, Y. Li, L. Zhu, and Y. Yao, "Robust attitude and positioning alignment methods for SINS/DVL integration based on sliding window improvements," *IEEE Transactions on Industrial Electronics*, vol. 71, no. 7, pp. 8038–8046, 2024, doi: 10.1109/TIE.2023.3294582.
- [25] X. Zhou, M. Zhang, J. Hu, L. Li, and X. Guan, "A robust in-motion coarse alignment method for low-accuracy SINS and GPS integrated system," *IEEE/ASME Transactions on Mechatronics*, vol. 30, no. 1, pp. 611–622, 2025, doi: 10.1109/TMECH.2024.3397244.
- [26] H. Huang, J. Wei, L. Zhang, B. Wang, and S. Wang, "A coarse alignment method based on vector observation and truncated vectorized κ -matrix for underwater vehicle," *IEEE Transactions on Vehicular Technology*, vol. 72, no. 3, pp. 3227–3238, 2023, doi: 10.1109/TVT.2022.3220293.
- [27] H. Zhou and X. Ye, "A unified initial alignment method of SINS based on FGO," *IEEE Transactions on Industrial Electronics*, vol. 70, no. 11, pp. 11795–11803, 2023, doi: 10.1109/TIE.2022.3229335.
- [28] H. Qin, X. Wang, G. Wang, M. Hu, Y. Bian, X. Qin, and R. Ding, "A fast in-motion alignment method for INS/DVL in rough sea conditions," *IEEE Transactions on Instrumentation and Measurement*, vol. 73, pp. 1–11, 2024, doi: 10.1109/TIM.2024.3481561.
- [29] F. Pei, Y. Su, D. Zhu, and S. Yin, "A novel coarse alignment method for SINS using special orthogonal group optimal estimation," *Sensors*, vol. 20, no. 20, Art. no. 5740, 2020, doi: 10.3390/s20205740.
- [30] L. Chang and Y. Luo, "Log-linear error state model derivation without approximation for INS," *IEEE Transactions on Aerospace and Electronic Systems*, vol. 59, no. 2, pp. 2029–2035, 2023, doi: 10.1109/TAES.2022.3197726.
- [31] F. Yue, L. Miao, and Z. Zhou, "An equivalent backtracking coarse alignment method with dynamic optimal sliding window integration," *Measurement*, vol. 256, Art. no. 118290, 2025, doi: 10.1016/j.measurement.2025.118290.
- [32] M. D. Shuster, "The TASTE test," *The Journal of the Astronautical Sciences*, vol. 57, no. 1, pp. 61–71, 2009, doi: 10.1007/BF03321494.
- [33] F. O. Silva, E. M. Hemerly, and W. C. L. Filho, "Error analysis of analytical coarse alignment formulations for stationary SINS," *IEEE Transactions on Aerospace and Electronic Systems*, vol. 52, no. 4, pp. 1777–1796, 2016, doi: 10.1109/TAES.2016.7738355.
- [34] F. O. Silva, "Generalized error analysis of analytical coarse alignment formulations for stationary SINS," *Aerospace Science and Technology*, vol. 79, pp. 500–505, 2018, doi: 10.1016/j.ast.2018.06.015.
- [35] F. O. Silva, E. M. Hemerly, W. C. L. Filho, and H. K. Kuga, "A fast in-field coarse alignment and bias estimation method for stationary intermediate-grade IMUs," *IEEE Transactions on Instrumentation and Measurement*, vol. 67, no. 4, pp. 831–838, 2018, doi: 10.1109/TIM.2017.2789138.
- [36] G. Chang, T. Xu, and Q. Wang, "Error analysis of Davenport's q method," *Automatica*, vol. 75, pp. 217–220, 2017, doi: 10.1016/j.automatica.2016.09.018.
- [37] Y. Cheng and J. L. Crassidis, "Optimal pose estimation with error-covariance analysis," in *Proc. AIAA Scitech 2021 Forum*, 2021, doi: 10.2514/6.2021-1758.
- [38] W. Ouyang and Y. Wu, "Optimization-based strapdown attitude alignment for high-accuracy systems: Covariance analysis with applications," *IEEE Transactions on Aerospace and Electronic Systems*, vol. 58, no. 5, pp. 4053–4069, 2022, doi: 10.1109/TAES.2022.3157570.